arXiv:2111.13923v1 [eess.IV] 27 Nov 2021

Learning A 3D-CNN and Transformer Prior for Hyperspectral Image Super-Resolution

Qing Ma[1] Junjun Jiang[1,2*] Xianming Liu[1,2] Jiayi Ma[3]
[1]Harbin Institute of Technology [2]Peng Cheng Laboratory [3]Wuhan University

Abstract

To solve the ill-posed problem of hyperspectral image super-resolution (HSISR), an usually method is to use the prior information of the hyperspectral images (HSIs) as a regularization term to constrain the objective function. Model-based methods using hand-crafted priors cannot fully characterize the properties of HSIs. Learning-based methods usually use a convolutional neural network (CNN) to learn the implicit priors of HSIs. However, the learning ability of CNN is limited, it only considers the spatial characteristics of the HSIs and ignores the spectral characteristics, and convolution is not effective for long-range dependency modeling. There is still a lot of room for improvement. In this paper, we propose a novel HSISR method that uses Transformer instead of CNN to learn the prior of HSIs. Specifically, we first use the proximal gradient algorithm to solve the HSISR model, and then use an unfolding network to simulate the iterative solution processes. The self-attention layer of Transformer makes it have the ability of spatial global interaction. In addition, we add 3D-CNN behind the Transformer layers to better explore the spatio-spectral correlation of HSIs. Both quantitative and visual results on two widely used HSI datasets and the real-world dataset demonstrate that the proposed method achieves a considerable gain compared to all the mainstream algorithms including the most competitive conventional methods and the recently proposed deep learning-based methods.

1. Introduction

Hyperspectral images (HSIs) have high spectral resolution and are widely used in various computer vision tasks, including target recognition and tracking [28, 33], medical image processing [1], and remote sensing [6, 17]. While the HSI can achieve a high spectral resolution with contiguous and narrow bands, its spatial resolution is usually much coarser than that of the RGB images in our daily life. This is due to the fact that the dense spectral bands in the hyperspectral sensors make a limited amount of photons reached one narrow spectral window averagely. The low spatial resolution of the HSI captured by the sensor greatly limits its value for application. A natural solution is to instead capture a low-resolution (LR) HSI and a high-resolution (HR) multispectral image (MSI), *e.g.*, RGB image, and fuse them into a resultant image with high spatial and spectral resolution simultaneously. This procedure is referred to as hyperspectral multispectral image fusion (HS/MS fusion) or hyperspectral super-resolution.

Traditional HS/MS fusion methods employ prior knowledge of HSIs as regularizer to solve such a seriously ill-posed problem, *e.g.*, sparse representation [2, 12, 21], low-rank prior [35, 51], non-local [8, 44, 52] and self-similarity [19]. They have achieved better and better performance, because these priors are getting closer and closer to the essential characteristics of the data. However, the prior knowledge is predefined manually and is born with the following shortcomings. On the one hand, a high level of wisdom is required. On the other hand, these hand-crafted priors have limitations and often fail to reflect all the characteristics of the data. These severely restrict the performance and generalization ability of the optimization-based methods mentioned above.

Given the recent advances in deep learning, many convolutional neural networks (CNNs) based image super-resolution approaches have garnered attention recently. To solve the above problems of traditional HS/MS fusion methods, some researchers use deep learning to cope with the fusion based HSISR problem. Unlike traditional methods of manually designing a prior, these deep learning-based methods embrace a large amount of data to learn data-driven priors, greatly improving the fusion performance. Researchers have proposed some specialized modules, such as spatial attentions, channel attentions, and joint ones, to exploit the spatial, spectral, or spatio-spectral priors of HSIs. To take advantage of the observation model and address the gap between the optimization-based and learning-based methods, most recently, a series of HS/MS fusion methods based on unfolding networks have been proposed. For example, Xie *et al.* [43] proposed an effective unfolding net-

*Corresponding author: jiangjunjun@hit.edu.cn

work based on MHF-net, which first constructs an MS/HS fusion model and then builds the proposed network by unfolding the proximal gradient algorithm to solve the proposed model. Wang *et al.* [37] proposed the DBIN model, where the estimation of the observation model and the fusion process is optimized iteratively and alternatively during the super-resolution reconstruction. Dong *et al.* [14] proposed an approach based on MoG-DCN, an iterative HSISR algorithm based on a deep HSI denoiser to leverage both domain knowledge likelihood and deep image prior. Essentially, these methods all try to cast the HS/MS fusion optimization problem into joint learning of the observation model and a deep denoiser prior. The intrinsic difference among the above three tasks lies in how to model the denoiser prior. MHF-net and DBIN stack several ResBlocks [20] to model the data prior, while MoG-DCN leverages a relatively complex U-net [30] to exploit the prior.

In this paper, we try to design a more powerful network that can fully extract the priors of HSIs. We observe that the HSIs are three-dimensional data cubes, and their priors can be divided into two aspects: spatial priors and spectral priors. We need to design appropriate networks for these two aspects to better learn the priors of HSIs. We propose to use Transformer [34] to learn the spatial prior of HSIs. The self-attention mechanism in the Transformer requires each pixel of the image to pay attention to each other pixel, so that Transformer has long-range modeling capabilities and has achieved good performance in many visual tasks. It is very suitable for extracting the spatial prior of HSIs. As for the spectral prior, 3D-CNN is a natural and effective choice. It can pay attention to the correlation of spatio-spectra while learning spectral priors. Keeping these in mind, we propose an HS/MS fusion model, namely 3D-CNN and Transformer prior network (3DT-Net). We first use the proximal gradient algorithm to solve the optimization problem with the observation models of LR-HSIs and HR-MSIs, and then we unfold the iterative process of the proximal gradient algorithm into a multistage network. Particularly, in each iteration, unlike previous learning-based methods that construct 2D-CNN to learn priors, we design a 3D-CNN and Transformer network with Swin Transformer layers [25] to exploit spatial priors and 3D convolutional layers to exploit spatio-spectral correlation priors. Experimental results have shown that the proposed 3DT-Net outperforms many recently proposed HS/MS fusion methods.

2. Related Work

In this section, we introduce related existing methods, particularly focusing prior modeling in hyperspectral image super-resolution and vision Transformer.

2.1. Prior Modeling in HSISR

HSIs super-resolution is an ill-posed problem, a common solution is to choose a prior or regularization to constrain the optimization equation. Various priors have been already exploited to regularize the HSIs Super-resolution problem. In [27], Frosti *et al.* used total variation to regularize an ill-posed problem dictated by a widely used explicit image formation model. Considering that HSIs are redundant in nature, sparse prior can be used to constrain the spatial and spectral correlation of HSIs. Wei *et al.* [40] designed a sparse regularization term, relying on a decomposition of the scene on a set of dictionaries. In [2], Akhtar *et al.* proposed a generic Bayesian sparse coding strategy to be used with Bayesian dictionaries learned with the Beta process. In addition, spectral unmixing prior [41, 47] and self-similarity [19] are also often used to address HSISR. The main drawback of these methods is the quality of the recovered HSIs highly depend on whether the selected prior is appropriate. In addition, it requires manual tweaking of its balancing parameters between the data term and prior term.

In recent years, deep learning have pushed forward the frontier of many computer vision tasks, including image classification and object detection [18, 20], image retrieval [29], and so on. Inspired by these representative work, using deep learning methods to accomplish the HS/MS fusion has attracted wide attention. Different from the traditional method of manual design a prior, the deep learning-based methods use a large amount of data to learn data-driven priors. Dian *et al.* [10] combined traditional methods with deep learning methods. They first initialize the HR-HSI by solving a Sylvester equation, and then use deep CNN to learn the priors of the target HR-HSI. Xie *et al.* [43] and Wu Wang *et al.* [37] used ResNet to learn HSIs priors. Dian *et al.* [11] proposed using a CNN denoiser to regularize the HS/MS fusion model. In [14], Dong *et al.* proposed using U-net to replace ResNet to learn a denoising prior for HS/MS fusion.

2.2. Vision Transformer

Transformer was proposed by Vaswani *et al.* [34] for NLP. Since directly replacing the CNN convolution layers with Transformer layers to process images will bring a huge computational burden, the early methods are to augment a standard CNN model with Transformer layers [5, 32, 38, 46]. Recently, Chen *et al.* [7] proposed a backbone model IPT for image restoration based on Transformer. However, IPT has a huge amount of parameters and calculations, and it is very difficult to train such a model. In order to solve the problem of large amount of calculation when using the Transformer to process image tasks, Dosovitskiy *et al.* [15] proposed to split the training image into a sequence of image patches. However, [15] cannot handle high-resolution images, due to its low-resolution feature maps and the

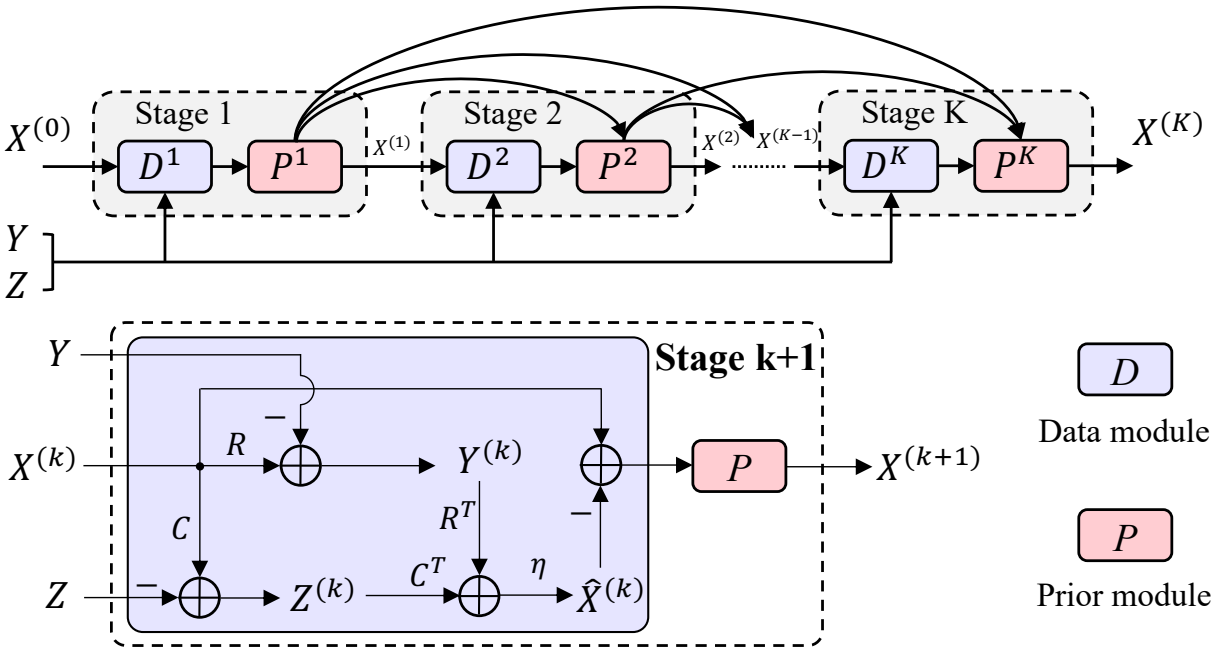


Figure 1. The flowchart of our proposed 3DT-Net deep unrolling framework.

quadratic increase in complexity with image size. Follow up [15], Liu *et al.* proposed Swin Transformer [25], a hierarchical Transformer whose representation is computed with Shifted windows. Swin Transformer can not only process high-resolution images like CNN, but also has the advantage of Transformer to model long-range dependency. In [24], an image restoration Transformer was developed based on Swin Transformer, which achieves state-of-the-art performance in various image reconstruction tasks.

3. Proposed Method

3.1. Model Formulation

In this paper, we use lowercase letters to denote scalars, use bold letters to denote matrices, and use curlycue to denote tensors. Specially, let $\mathcal{Y} \in \mathbb{R}^{W\times H\times s}$ represent the HR-MSI and $\mathcal{Z} \in \mathbb{R}^{w\times h\times S}$ represent the LR-HSI. The goal of HSISR is to combine information coming from an LR-HSI and an HR-MSI. The former has high spectral resolution, with S spectral bands, but low geometric resolution with w and h being image width and height, respectively. The latter has high spatial resolution with W and H being image width and height, respectively, but a low spectral resolution s. We aim to estimate a fused image $\mathcal{X} \in \mathbb{R}^{W\times H\times S}$ with both high spatial and high spectral resolution.

If we reshape the spatio-spectral data-cube $\mathcal{Y}$, $\mathcal{Z}$ and $\mathcal{X}$ to their matrix formulations, *i.e.*, $\boldsymbol{Y} \in \mathbb{R}^{WH\times s}$, $\boldsymbol{Z} \in \mathbb{R}^{wh\times S}$, and $\boldsymbol{X} \in \mathbb{R}^{WH\times S}$, the observation models for the HR-MSI and LR-HSI can be written as follows:

$$\boldsymbol{Y} = \boldsymbol{X}\boldsymbol{R}, \tag{1}$$

$$\boldsymbol{Z} = \boldsymbol{C}\boldsymbol{X}. \tag{2}$$

where $\boldsymbol{R} \in \mathbb{R}^{S\times s}$ is the spectral response function of the multispectral sensor, $\boldsymbol{C} \in \mathbb{R}^{wh\times WH}$ represents the degradation operator which is often assumed to be composed of a cyclic convolution operator and a down-sampling matrix. We can obtain $\boldsymbol{X}$ by solving the following optimization problem

$$\min_{\boldsymbol{X}} \ \frac{1}{2}\|\boldsymbol{X}\boldsymbol{R}-\boldsymbol{Y}\|_F^2 + \frac{1}{2}\|\boldsymbol{C}\boldsymbol{X}-\boldsymbol{Z}\|_F^2 + \lambda f(\boldsymbol{X}). \tag{3}$$

where the first and second terms are fidelity terms and the third term is a regularization term which represents prior knowledge of $\boldsymbol{X}$. In the conventional HS/MS fusion methods, most of the priors are hand-crafted based on empirical observation, such as sparse priors [12, 21], low-rank priors [35, 51], self-similarity [19]. Although they have achieved promising results, but they only use a certain property of hyperspectral images, and it is difficult to apply to a variety of hyperspectral images. Pioneering works [14, 37, 43] have proved that the performance of data-driven priors exceeds that of hand-crafted priors. Therefore, in this work, we use a network to learn the data-driven implicit prior.

Since the specific form of the prior is not specified, the regularization term is usually non-smooth and non-differentiable functions of the outputs. Therefore, in this paper we use a proximal gradient algorithm [4] to solve Eq.

(3). Let $\mathcal{L}(\boldsymbol{X}) = g(\boldsymbol{X}) + \lambda f(\boldsymbol{X})$, where $g(\boldsymbol{X})$ is differentiable (includes the first two terms of Eq. (3)) and $\lambda f(\boldsymbol{X})$ is non-differentiable. The proximal gradient algorithm minimizes Eq. (3) by iterating the following equation until convergence:

$$\boldsymbol{X}^{(k+1)} = \text{prox}_{\lambda\eta f}(\boldsymbol{X}^{(k)} - \eta \bigtriangledown g(\boldsymbol{X}^{(k)})), \tag{4}$$

where η plays the role of step size, and $\text{prox}_{\lambda\eta f}(\cdot)$ is a proximal operator dependent on λ, η and f. Since $\bigtriangledown g(\boldsymbol{X}^{(k)}) = (\boldsymbol{X}^{(k)}\boldsymbol{R} - \boldsymbol{Y})\boldsymbol{R}^T + \boldsymbol{C}^T(\boldsymbol{C}\boldsymbol{X} - \boldsymbol{Z})$, we substitute it into Eq. (4) to obtain the following optimization problem that can be solved iteratively:

$$\boldsymbol{X}^{(k+1)} = \text{prox}_{\lambda\eta f}(\boldsymbol{X}^{(k)} - \eta(\boldsymbol{X}^{(k)}\boldsymbol{R} - \boldsymbol{Y})\boldsymbol{R}^T + \boldsymbol{C}^T(\boldsymbol{C}\boldsymbol{X}^{(k)} - \boldsymbol{Z})). \tag{5}$$

3.2. Optimization-based Unfolding Network

Conventional proximal gradient algorithm requires many iterations to converge and is computationally expensive. Moreover, the step size η has to be selected by hand and it is difficult to find the optimal η. To overcome these shortcomings, recent works [13, 14, 43] used a deep unfolding network to unfold the iterative optimization steps into a series of networks. These models have been trend-setting and promising in solving the inverse problems. The methods based on deep unfolding strategy have the fundamental advantages of interpretability, fewer parameters, and fast convergence. We derive our motivation from these works and design a deep unfolding network to solve the optimization Eq. (5).

Before solving Eq. (5), we first present the physical meaning of matrix operations in this paper: the left multiplication matrix represents the spatial transformation of the input, and the right multiplication matrix represents the channel transformation of the input. Then we unfold the iteration Eq. (5) into the following equivalent four sequential parts:

$$\boldsymbol{Y}^{(k)} = \boldsymbol{X}^{(k)}\boldsymbol{R} - \boldsymbol{Y}, \tag{6}$$

$$\boldsymbol{Z}^{(k)} = \boldsymbol{C}\boldsymbol{X}^{(k)} - \boldsymbol{Z}, \tag{7}$$

$$\hat{\boldsymbol{X}}^{(k)} = \eta(\boldsymbol{Y}^{(k)}\boldsymbol{R}^T + \boldsymbol{C}^T\boldsymbol{Z}^{(k)}), \tag{8}$$

$$\boldsymbol{X}^{(k+1)} = \text{prox}_{\lambda\eta f}(\boldsymbol{X}^{(k)} - \hat{\boldsymbol{X}}^{(k)}), \tag{9}$$

where in Eq. (6), $\boldsymbol{R} \in \mathbb{R}^{S\times s}$ represents channel decrease operator, which can be performed by using some convolution layers. The simplest way is to apply the 1×1 convolution to decrease the channel number from S to s. In this paper, we leverage the more flexible 3×3 convolution layer to achieve this. In Eq. (7), $\boldsymbol{C} \in \mathbb{R}^{wh\times WH}$ represents the spatial downsampling operator, we perform it by several 2D convolution layers with kernel stride 2 and thus each 2D convolution layer carrying out 2 times downsampling. $\boldsymbol{R}^T \in \mathbb{R}^{s\times S}$ in Eq. (8) represents channel increase operator, we perform it by using the 3×3 convolution layers in a similar vein. $\boldsymbol{C}^T \in \mathbb{R}^{HW\times wh}$ represents an upsampling operator, and we perform it by several 2D transposed convolution layers [16] with each 2D transposed convolution layer carrying out 2 times upsampling. Since it is almost impossible to find the best η by hand, we set η to be a learnable parameter and update it as the backward propagation of errors. In Eq. (9), $\text{prox}_{\lambda\eta f}(\cdot)$ is a proximal operator used to model the image prior. For the simple prior modeling, such as the l-norm regularization for sparse representation, the proximal is tractable and can be modeled in closed-form through soft-thresholding and shrinkage based unrolling network [50]. More details about the prior network will be introduced in the next section.

Motivated by the proximal gradient iterations in Eq. (6)-(9), we can now perform these invert linear inverse tasks by efficient network architectures. Fig. 1 shows the architecture of the proposed network. The observations Y and Z forms the inputs for all iterations, which together with the output $X^{(k)}$ of the previous iteration form the variable for the current iteration. The network contains K iteration stages, and each iteration stage is composed of a data module (corresponding to Eq. (6)-(8)) and a prior module (corresponding to Eq. (6)-(9)), which is modeled via an efficient network architecture, as will be elaborated in the next section. In the first stage (*i.e.*, $k = 1$), we perform Bicubic upsampling on LR-HSI Z to initialize $\boldsymbol{X}^{(0)}$. To reduce the number of parameters, we share the parameters for different stages. Therefore, the proximal map will be modeled by unrolling the proximal gradient iterations through a recurrent-like architecture [26]. To avoid information loss during transmissions between iterations, inspired by some previous works [14, 42] we propose to densely connect the hierarchical feature maps from the previous prior module to the subsequent prior modules, as shown in Fig. 1.

3.3. 3D-CNN and Transformer Prior Network

For these deep unfolding networks, the proximal operator is usually modeled as a deep neural model, which resembles the projection from the (noisy) observation onto the manifold (where the true image lies in) of visually plausible images. Therefore, the proximal operator can be seen as a denoiser that gradually removes the artifacts from the noisy observation. Pioneering works (*e.g.*, DBIN [37], MHF-net [43], MoG-DCN [14] *etc.*) usually used a subnetwork to learn this operation. In DBIN [37] and MHF-net [43], the authors adopted ResNet to learn this proximal operator and attained satisfactory performance. Recently, MoG-DCN [14] proposed to use U-net [30] as the backbone network architecture to learn this proximal operator which achieves the SOTA performance on the HS/MS fusion task.

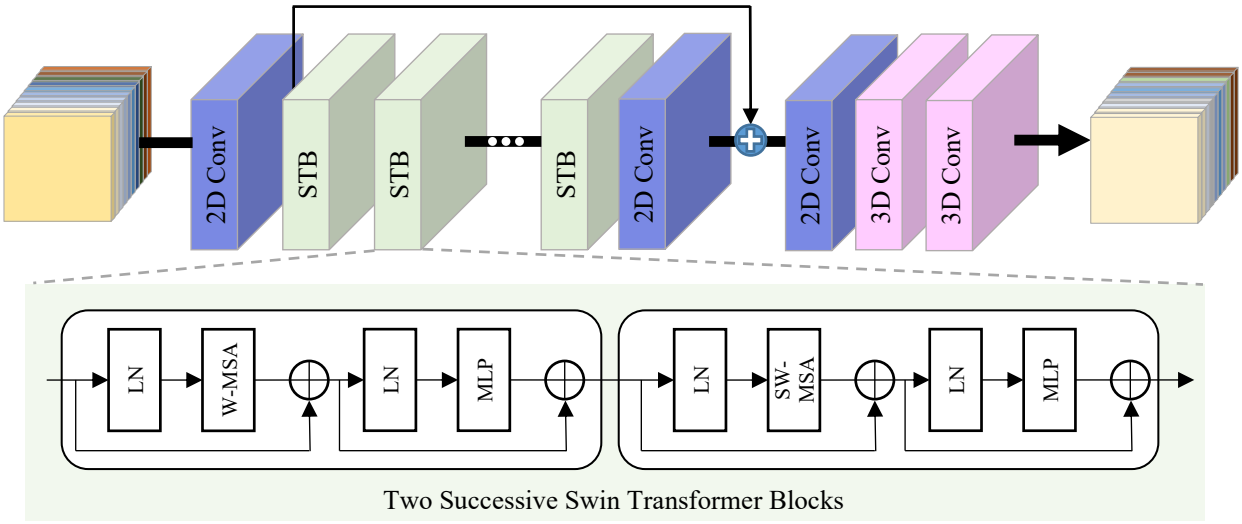


Figure 2. Illustration of the network architecture of the proposed 3D-CNN and Transformer Prior (3DT) module. LN and MLP, are the LayerNorm and MultiLayer Perceptron layers, respectively. W-MSA and SW-MSA represent the window based multi-head self-attention using regular and shifted window partitioning configurations, respectively.

From these works, it is easy to analyze that the performance of the selected prior estimation network is the essential factor that determines the performance of the entire HS/MS fusion network. Therefore, in this paper, we take the existing method one step further and propose a new denoiser prior learning network based on 3D-CNN and Transformer network, which introduces the powerful Transformer [34] structure into the prior learning network.

The architecture of the 3D-CNN and Transformer prior network is illustrated in Fig. 2. The main components of the 3D-CNN and Transformer prior network are Swin Transformer layer (STL) and 3D convolution layer. The STL was proposed for the first time in [25]. It has long-range modeling capabilities like the original Transformer, and the amount of calculations is much smaller than that of the original Transformer. Therefore, it is a very good choice for learning data priors. However, STL is designed for natural RGB images. It fully considers the spatial self-similarity of the image, but does not consider the spectral correlation of the HSI data. Therefore, it is not appropriate to directly use STL to learn the priors of 3D HSIs. To address this problem, we use 3D convolutional layers to learn the spectral priors of HSIs. Compared with filters in 2D convolution, filters in 3D convolution are more flexible in the channel dimension, making it more suitable for exploring the spatio-spectral correlation of HSIs.

3.4. Training Details

We resort to the L_1 loss to train our network

$$L = \|\boldsymbol{X}^{(K)} - \boldsymbol{X}\|_1, \tag{10}$$

where $\boldsymbol{X}^{(K)}$ is the final output HR-HSI. $\boldsymbol{X}$ is the ground truth HR-HSI.

In our implementation, we initialize η with a uniform distribution in $[0, 1]$ and in each stage are updated with gradient-based method. We use Adam optimizer [22] with $\beta_1 = 0.9$, $\beta_2 = 0.999$, $\epsilon = 10^{-8}$ to train the network for 250000 iterations with a batch size of 8. We set each epoch to have 2500 iterations, thus there are 100 epochs. The learning rate is initialized as 0.0001. We implement and train our network using Pytorch framework with an NVIDIA Tesla V100 GPU.

4. Experiments and Analyses

In this section, we compare our proposed method with eight other state-of-the-art methods including four traditional methods, *e.g.*, Hysure [31][1], NSSR [12][2], CSTF [23][3], LTTR [9][4], and four recently proposed deep learning-based methods, *e.g.*, CNN-FUS [11][5], MHF-net [43][6], DBIN [37][7], MoG-DCN [14][8]. As for objective comparisons, we use four picture quality indices (PQIs) to evaluate the performance of different methods, including peak signal-to-noise ratio (PSNR), SAM [48], erreur relative

[1]https://github.com/alfaiate/HySure
[2]http://see.xidian.edu.cn/faculty/wsdong/HSI_SR_Project.htm
[3]https://github.com/renweidian/CSTF
[4]https://github.com/renweidian/LTTR
[5]https://github.com/renweidian/CNN-FUS
[6]https://github.com/XieQi2015/MHF-net
[7]https://github.com/wwhappylife/Deep-Blind-Hyperspectral-Image-Fusion
[8]https://github.com/chengerr/Model-Guided-Deep-Hyperspectral-Image-Super-resolution

Table 1. Influence of the number of iterations for our 3DT-Net.

Model	PSNR	SAM	ERGAS	SSIM
3DT-Net ($K = 1$)	49.35	2.40	0.53	0.995
3DT-Net ($K = 2$)	50.26	2.13	0.50	**0.996**
3DT-Net ($K = 3$)	**50.93**	**2.01**	**0.45**	**0.996**
3DT-Net ($K = 4$)	50.91	2.05	0.46	**0.996**

Table 2. Ablation study on the prior network with different setting.

Network	Para(M)	PSNR	SAM	ERGAS	SSIM
ResNet	6.75	48.29	2.51	0.60	0.995
U-net	6.70	49.71	2.28	0.50	**0.996**
Transformer	3.46	50.76	2.07	0.46	**0.996**
3DT-Net	3.46	**50.93**	**2.01**	**0.45**	**0.996**

globale adimensionnelle de synthèse (ERGAS) [36] and structure similarity (SSIM) [39]. PSNR and SSIM are calculated on each 2D spatial image, which evaluate the similarity between the recovered HSI and the ground truth based on MSE and structural consistency, respectively. SAM calculates the average angle between spectrum vectors of the recovered HSI and the ground truth. ERGAS reflects the overall quality of the recovered HSI. Smaller values of ERGAS and SAM suggest better results, while larger values of PSNR and SSIM imply better results.

4.1. Training Datasets

We evaluate our proposed method on two publicly simulated hyperspectral imaging datasets including the *CAVE* [45][9] and the *Harvard* [3][10]. For real data experiments, we use *WV-2*[11].

The CAVE database consists of 32 indoor images captured under controlled illumination with spatial size of 512×512, including 31 spectral bands of 10 nm wide, covering the visible spectrum from 400 to 700nm. We follow the same setting as [14], the HR-MSI (RGB image) is generated by integrating all the ground truth HR-HSI bands with the same simulated spectral response function R of a Nikon D700 camera[12], and the LR-HSI can obtained by first applying an anti-aliasing 8×8 Gaussian filter with a standard deviation of 2 to the original HR-HSIs followed by a downsampling along both the horizontal and vertical dimensions with the scaling factor of 8. We select the first 20 samples and randomly extract 64×64 overlapped patches from them as reference HR-HSIs for training. Thus, the HR-HSIs, HR-MSIs and LR-HSIs are of sizes $64 \times 64 \times 31$, $64 \times 64 \times 3$, $8 \times 8 \times 31$, respectively. The remaining 12 samples of the database are used for testing.

The Harvard database contains 50 indoor and outdoor images recorded under daylight illumination with spatial size of $1,040 \times 1,392$, including 31 spectral bands of 10 nm wide, covering the visible spectrum from 400 to 700nm. Then we use the same method as CAVE database to get the HR-MSI and LR-HSI. We select the first 30 samples and randomly extract 64×64 overlapped patches from them as reference HR-HSIs for training. Thus, the HR-HSIs, HR-MSIs and LR-HSIs are of sizes $64 \times 64 \times 31$, $64 \times 64 \times 3$, $8 \times 8 \times 31$, respectively. The remaining 20 samples of the database are used for testing.

The WV-2 database contains a LR-HSI of size $419 \times 658 \times 8$ and an HR-MSI of size $1676 \times 2632 \times 3$, while the ground truth HR-HSI is unavailable. We follow the same setting as [43] to generate the training data. We select the top half part of the HR-MSI $836 \times 2632 \times 3$ and LR-HSI $209 \times 658 \times 8$ as training data and exploit the remaining parts of the data set as testing data. We use the Wald's protocol [49] to generate the training samples. We divide the training data into $256\times256\times3$ overlapped HR-MSI patches and $64\times64\times8$ overlapped LR-HSI patches. Then we downsampling HR-MSI and LR-HSI patches into size $64\times64\times3$ and $16 \times 16 \times 8$ as the input HR-MSI and LR-HSI, respectively. Note that the original $64 \times 64 \times 8$ HSI is taken as ground truth.

4.2. Ablation Study

In this section, we conduct simulated experiments to show the effectiveness of our network in three aspects: the influence of stage number K, the effectiveness of 3D-CNN and Transformer prior network, and the effectiveness of 3D-CNN over 2D-CNN.

Effect of stage number K. To explore the impact of the number of unfolded stages on the HSISR performance, we report the performance of the proposed 3DT-Net with different stage number K. Table 1 shows the average results over 12 testing HSIs. Here, the bold values represent the best result, and the results with underlines denote the second best. From the table, we can observe that as the number of iterations increases, the performance of PSNR and SSIM will increase, but when $K>3$, the performance of PSNR and SSIM will decrease. This shows that our method can quickly converge after several iterations, but the performance may not be improved when the iteration is increased, because the network is too complex and it will be difficult to train to obtain the optimal solution. In the following experiments, we choose $K = 3$ in our implementation.

Effect of 3D-CNN and Transformer prior network. To verify the effectiveness of 3D-CNN and Transformer prior

[9] http://www.cs.columbia.edu/CAVE/databases/

[10] http://vision.seas.harvard.edu/hyperspec/d2x5g3/

[11] https://www.harrisgeospatial.com/Data-Imagery/Satellite-Imagery/High-Resolution/WorldView-2

[12] http://www.maxmax.com/spectral_response.htm

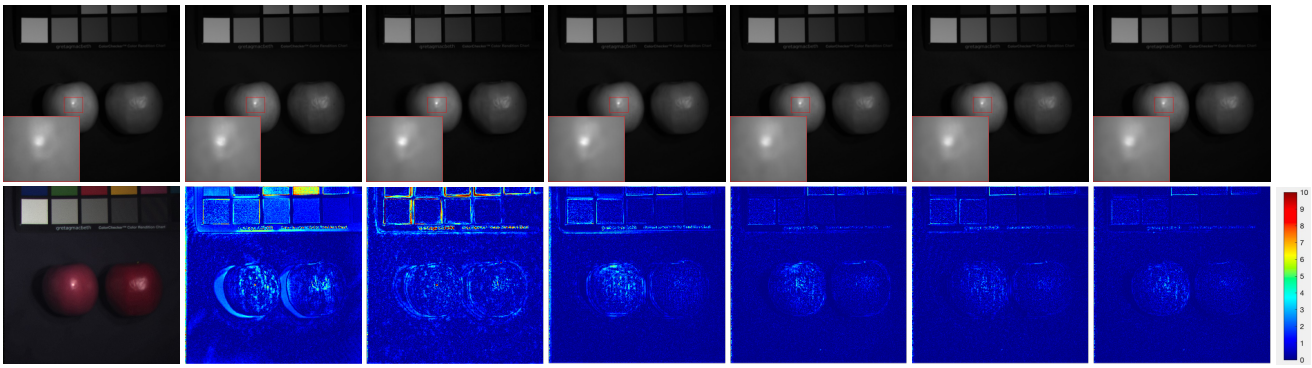


Figure 3. Qualitative results of the CAVE datasets at band 31. Top row: Ground truth and reconstructed images by 6 comparison methods, with a demarcated areas zoomed in 4 times for easy observation. Bottom row: RGB and the error images of the result obtain by the 6 competing methods.

Table 3. Quantitative comparisons of different approaches over 10 testing images from the CAVE dataset with respect to four PQIs.

Method	PSNR	SAM	ERGAS	SSIM
Hysure [31]	40.06	9.66	1.30	0.976
NSSR [12]	44.07	4.35	0.82	0.987
CSTF [23]	42.41	5.04	0.87	0.979
LTTR [9]	45.89	2.97	0.66	0.994
CNN-FUS [11]	44.21	4.04	0.82	0.989
MHF-net [43]	46.31	3.39	0.64	0.994
DBIN [37]	48.82	2.09	0.50	**0.996**
MoG-DCN [14]	49.89	2.04	**0.45**	**0.996**
3DT-Net	**50.93**	**2.01**	**0.45**	**0.996**

Table 4. Quantitative comparisons of different approaches over 20 testing images from the Harvard dataset with respect to four PQIs.

Method	PSNR	SAM	ERGAS	SSIM
Hysure [31]	44.26	3.75	1.40	0.983
NSSR [12]	46.08	3.40	1.20	0.985
CSTF [23]	44.98	3.54	1.07	0.980
LTTR [9]	46.86	2.90	1.11	0.987
CNN-FUS [11]	46.05	3.24	1.12	0.985
MHF-net [43]	46.42	3.01	1.09	0.987
DBIN [37]	47.36	2.71	0.97	0.988
MoG-DCN [14]	47.64	2.67	0.91	0.988
3DT-Net	**48.05**	**2.27**	**0.84**	**0.991**

network, we use the ResNet prior network adopted in [37, 43] and U-net prior network adopted in [14] to replace the proposed 3D-CNN and Transformer prior network, respectively. Considering the powerful long-range modeling ability of Transformer, it only needs very few parameters to achieve strong performance. We use the U-net prior network proposed in [14] as the best U-net prior network (its parameter amount may lager than our method), rather than requiring that the parameters of the U-net prior network must be the same as these of the 3D-CNN and Transformer prior network. For fair comparison of ResNet, we let the parameters of ResNet prior network the same as the U-net prior network. From Table 2, we can see that the PSNR value of Transformer prior network is 1.05 dB higher than that of the U-net prior network, and the parameters are only half of the U-net prior network. After the introduction of 3D convolutional layers (the only difference between Transformer and 3DT-Net), the PSNR performance increased again by 0.17 dB, which proves that 3D convolutional layers can better extract the spatio-spectral correlation priors.

4.3. Experiments with Simulated Data

The average results in terms of the PSNR, SAM, ERGAS and SSIM of all the competing methods on the CAVE and Harvard datasets are reported in Table 3 and Table 4, respectively. From these two tables, it can be seen that the performance of deep learning-based methods are better than that of traditional shallow learning-based methods, which shows the advantages and representation ability of deep neural networks. Clearly, the proposed 3DT-Net method outperforms all other competing methods by a considerable margin. The average PSNR value of our method is more than 1.0 dB and 0.4 dB higher than that of the second best method (*i.e.*, the MoG-DCN method) on CAVE and Harvard datasets, respectively.

In Fig. 3 and Fig. 4, we show parts of the reconstructed HR-HSIs at 700 nm by the competing methods for the test image *real and fake apples* from the CAVE dataset and the test image *imgf2* from the Harvard dataset, respectively. From Fig. 3, we can see that the composite image obtained by 3DT-Net is the closest to the ground-truth, while the re-

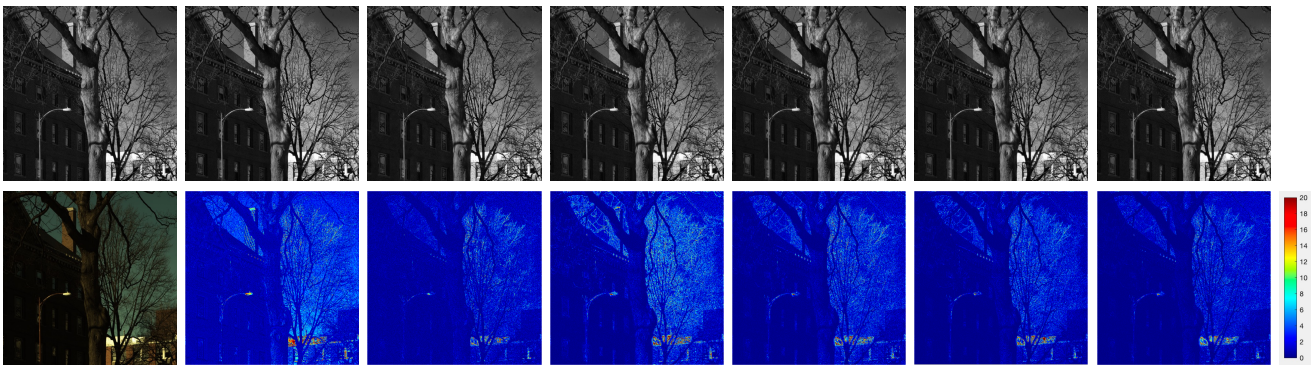


Figure 4. Qualitative results of the Harvard datasets at band 31. Top row: Ground truth and reconstructed images by 6 comparison methods. Bottom row: RGB and the error images of the result obtain by the 6 competing methods.

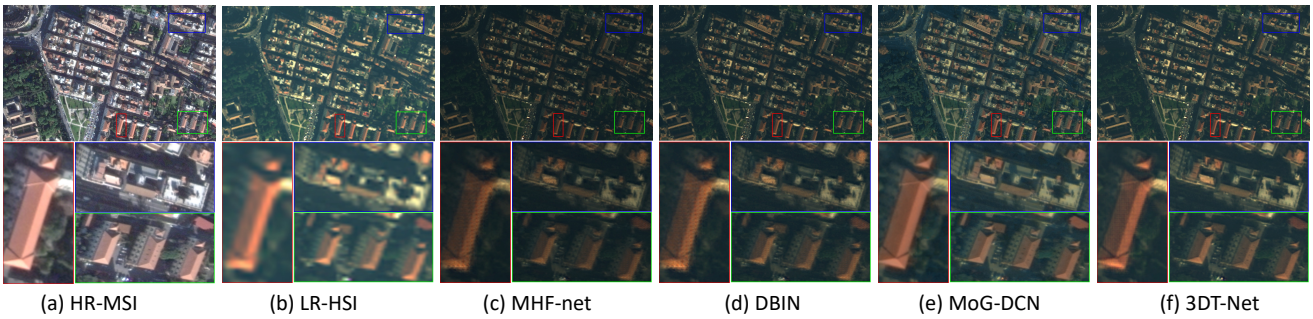


Figure 5. Qualitative results of the WV-2 dataset. (a) and (b) are the HR-MSI and LR-HSI of the right bottom area of Roman Colosseum. We show the composite image of the HSI with bands 5-3-2 as R-G-B. (c)-(f) reconstructed images by 6 comparison methods, with a demarcated areas zoomed for easy observation.

sults of Hysure and CNN-FUS contain obvious incorrect structure or spectral distortion. From Fig. 4, we can see that all the test methods can well reconstruct the HR spatial structures of the HSI. Obviously, the proposed method performs best in recovering the details of the original HSI and achieves the smallest reconstruction error.

4.4. Experiments with Real Data

To verify the robustness of our method on real data, a public dataset of real MSIs called WV-2 are used in our experiments. In Fig. 5, we show a portion of the fusion result of the testing data. It can be seen that MHF-net [43] and DBIN [37] have obvious blur and artifacts. Visual inspection clearly shows that the proposed method has better visual effect.

5. Conclusions

In this paper, we have provided a new deep unfolding network for hyperspectral image super-resolution based on proximal gradient algorithm and Transformer prior. Unlike other deep learning-based HSI super-resolution methods using CNN to learn the prior of HSIs, our 3DT-Net use Transformer layers to exploit spatial priors and 3D convolutional layers to exploit spatio-spectral correlation priors. Compared with CNN, Transformer has long-range modeling capabilities and can use fewer parameters to achieve better performance. 3D convolution slides along the spatial and channel dimensions at the same time, making it more suitable for exploring the spatio-spectral correlation of HSIs. Evaluations on two public simulated datasets and one real datasets both demonstrate that the proposed 3DT-Net achieves state-of-the-art performance in terms of quantitative result and visual quality.

The proposed prior modeling method is general for many low-level image restoration tasks. In particular, it can be seamlessly integrated with any method under the Plug-and-Play framework, especially suitable for processing high-dimensional data, such as hyperspectral image, video, and light-field. The limitation of our approach is that it is a little more computationally taxing than those convolutional residual block based network. Therefore, in the future we will exploit some efficient implementations to extend our method to other tasks.

References

[1] Hamed Akbari, Luma Halig, David M Schuster, Baowei Fei, Adeboye Osunkoya, Viraj Master, Peter Nieh, and Georgia Chen. Hyperspectral imaging and quantitative analysis for prostate cancer detection. *Journal of Biomedical Optics*, 17(7):076005, 2012. 1

[2] Naveed Akhtar, Faisal Shafait, and Ajmal Mian. Bayesian sparse representation for hyperspectral image super resolution. In *Proceedings of the IEEE Conference on Computer Vision and Pattern Recognition*, pages 3631–3640, 2015. 1, 2

[3] Boaz Arad, Radu Timofte, Ohad Ben-Shahar, Yi-Tun Lin, and Graham D Finlayson. Ntire 2020 challenge on spectral reconstruction from an rgb image. In *Proceedings of the IEEE Conference on Computer Vision and Pattern Recognition Workshops*, pages 446–447, 2020. 6

[4] Amir Beck and Marc Teboulle. A fast iterative shrinkage-thresholding algorithm for linear inverse problems. *SIAM journal on imaging sciences*, 2(1):183–202, 2009. 3

[5] Irwan Bello, Barret Zoph, Ashish Vaswani, Jonathon Shlens, and Quoc V Le. Attention augmented convolutional networks. In *Proceedings of the IEEE/CVF international conference on computer vision*, pages 3286–3295, 2019. 2

[6] Gustavo Camps-Valls, Devis Tuia, Lorenzo Bruzzone, and Jon Atli Benediktsson. Advances in hyperspectral image classification: Earth monitoring with statistical learning methods. *IEEE Signal Processing Magazine*, 31(1):45–54, 2013. 1

[7] Hanting Chen, Yunhe Wang, Tianyu Guo, Chang Xu, Yiping Deng, Zhenhua Liu, Siwei Ma, Chunjing Xu, Chao Xu, and Wen Gao. Pre-trained image processing transformer. In *Proceedings of the IEEE/CVF Conference on Computer Vision and Pattern Recognition*, pages 12299–12310, 2021. 2

[8] Renwei Dian, Leyuan Fang, and Shutao Li. Hyperspectral image super-resolution via non-local sparse tensor factorization. In *Proceedings of the IEEE Conference on Computer Vision and Pattern Recognition*, pages 5344–5353, 2017. 1

[9] Renwei Dian, Shutao Li, and Leyuan Fang. Learning a low tensor-train rank representation for hyperspectral image super-resolution. *IEEE transactions on neural networks and learning systems*, 30(9):2672–2683, 2019. 5, 7

[10] Renwei Dian, Shutao Li, Anjing Guo, and Leyuan Fang. Deep hyperspectral image sharpening. *IEEE Transactions on Neural Networks and Learning Systems*, (99):1–11, 2018. 2

[11] Renwei Dian, Shutao Li, and Xudong Kang. Regularizing hyperspectral and multispectral image fusion by cnn denoiser. *IEEE transactions on neural networks and learning systems*, 32(3):1124–1135, 2020. 2, 5, 7

[12] Weisheng Dong, Fazuo Fu, Guangming Shi, Xun Cao, Jinjian Wu, Guangyu Li, and Xin Li. Hyperspectral image super-resolution via non-negative structured sparse representation. *IEEE Transactions on Image Processing*, 25(5):2337–2352, 2016. 1, 3, 5, 7

[13] Weisheng Dong, Peiyao Wang, Wotao Yin, Guangming Shi, Fangfang Wu, and Xiaotong Lu. Denoising prior driven deep neural network for image restoration. *IEEE transactions on pattern analysis and machine intelligence*, 41(10):2305–2318, 2018. 4

[14] Weisheng Dong, Chen Zhou, Fangfang Wu, Jinjian Wu, Guangming Shi, and Xin Li. Model-guided deep hyperspectral image super-resolution. *IEEE Transactions on Image Processing*, 2021. 2, 3, 4, 5, 6, 7

[15] Alexey Dosovitskiy, Lucas Beyer, Alexander Kolesnikov, Dirk Weissenborn, Xiaohua Zhai, Thomas Unterthiner, Mostafa Dehghani, Matthias Minderer, Georg Heigold, Sylvain Gelly, et al. An image is worth 16x16 words: Transformers for image recognition at scale. In *International Conference on Learning Representations*, 2020. 2, 3

[16] Vincent Dumoulin and Francesco Visin. A guide to convolution arithmetic for deep learning. *arXiv preprint arXiv:1603.07285*, 2016. 4

[17] Mathieu Fauvel, Yuliya Tarabalka, Jon Atli Benediktsson, Jocelyn Chanussot, and James C Tilton. Advances in spectral-spatial classification of hyperspectral images. *Proceedings of the IEEE*, 101(3):652–675, 2012. 1

[18] Ross Girshick, Jeff Donahue, Trevor Darrell, and Jitendra Malik. Rich feature hierarchies for accurate object detection and semantic segmentation. In *Proceedings of the IEEE Conference on Computer Vision and Pattern Recognition*, pages 580–587, 2014. 2

[19] Xian-Hua Han, Boxin Shi, and Yinqiang Zheng. Self-similarity constrained sparse representation for hyperspectral image super-resolution. *IEEE Transactions on Image Processing*, 27(11):5625–5637, 2018. 1, 2, 3

[20] Kaiming He, Xiangyu Zhang, Shaoqing Ren, and Jian Sun. Deep residual learning for image recognition. In *Proceedings of the IEEE conference on computer vision and pattern recognition*, pages 770–778, 2016. 2

[21] Rei Kawakami, Yasuyuki Matsushita, John Wright, Moshe Ben-Ezra, Yu-Wing Tai, and Katsushi Ikeuchi. High-resolution hyperspectral imaging via matrix factorization. In *Proceedings of the IEEE Conference on Computer Vision and Pattern Recognition*, pages 2329–2336, 2011. 1, 3

[22] Diederik P Kingma and Jimmy Ba. Adam: A method for stochastic optimization. *arXiv preprint arXiv:1412.6980*, 2014. 5

[23] Shutao Li, Renwei Dian, Leyuan Fang, and José M Bioucas-Dias. Fusing hyperspectral and multispectral images via coupled sparse tensor factorization. *IEEE Transactions on Image Processing*, 27(8):4118–4130, 2018. 5, 7

[24] Jingyun Liang, Jiezhang Cao, Guolei Sun, Kai Zhang, Luc Van Gool, and Radu Timofte. Swinir: Image restoration using swin transformer. In *Proceedings of the IEEE/CVF International Conference on Computer Vision*, pages 1833–1844, 2021. 3

[25] Ze Liu, Yutong Lin, Yue Cao, Han Hu, Yixuan Wei, Zheng Zhang, Stephen Lin, and Baining Guo. Swin transformer: Hierarchical vision transformer using shifted windows. *arXiv preprint arXiv:2103.14030*, 2021. 2, 3, 5

[26] Morteza Mardani, Qingyun Sun, Shreyas Vasawanala, Vardan Papyan, Hatef Monajemi, John Pauly, and David Donoho. Neural proximal gradient descent for compressive imaging. *arXiv preprint arXiv:1806.03963*, 2018. 4

[27] Frosti Palsson, Johannes R Sveinsson, and Magnus O Ulfarsson. A new pansharpening algorithm based on total variation. *IEEE Geoscience and Remote Sensing Letters*, 11(1):318–322, 2013. 2

[28] Zhihong Pan, Glenn Healey, Manish Prasad, and Bruce Tromberg. Face recognition in hyperspectral images. *IEEE Transactions on Pattern Analysis and Machine Intelligence*, 25(12):1552–1560, 2003. 1

[29] Adnan Qayyum, Syed Muhammad Anwar, Muhammad Awais, and Muhammad Majid. Medical image retrieval using deep convolutional neural network. *Neurocomputing*, 266:8–20, 2017. 2

[30] Olaf Ronneberger, Philipp Fischer, and Thomas Brox. U-net: Convolutional networks for biomedical image segmentation. In *International Conference on Medical image computing and computer-assisted intervention*, pages 234–241. Springer, 2015. 2, 4

[31] Miguel Simoes, José Bioucas-Dias, Luis B Almeida, and Jocelyn Chanussot. A convex formulation for hyperspectral image superresolution via subspace-based regularization. *IEEE Transactions on Geoscience and Remote Sensing*, 53(6):3373–3388, 2014. 5, 7

[32] Aravind Srinivas, Tsung-Yi Lin, Niki Parmar, Jonathon Shlens, Pieter Abbeel, and Ashish Vaswani. Bottleneck transformers for visual recognition. In *Proceedings of the IEEE/CVF Conference on Computer Vision and Pattern Recognition*, pages 16519–16529, 2021. 2

[33] Hien Van Nguyen, Amit Banerjee, and Rama Chellappa. Tracking via object reflectance using a hyperspectral video camera. In *Proceedings of the IEEE Conference on Computer Vision and Pattern Recognition Workshops*, pages 44–51, 2010. 1

[34] Ashish Vaswani, Noam Shazeer, Niki Parmar, Jakob Uszkoreit, Llion Jones, Aidan N Gomez, Łukasz Kaiser, and Illia Polosukhin. Attention is all you need. In *Advances in neural information processing systems*, pages 5998–6008, 2017. 2, 5

[35] Miguel A Veganzones, Miguel Simoes, Giorgio Licciardi, Naoto Yokoya, José M Bioucas-Dias, and Jocelyn Chanussot. Hyperspectral super-resolution of locally low rank images from complementary multisource data. *IEEE Transactions on Image Processing*, 25(1):274–288, 2015. 1, 3

[36] Lucien Wald. *Data fusion: definitions and architectures: fusion of images of different spatial resolutions*. Presses des MINES, 2002. 6

[37] Wu Wang, Weihong Zeng, Yue Huang, Xinghao Ding, and John Paisley. Deep blind hyperspectral image fusion. In *Proceedings of the IEEE International Conference on Computer Vision*, pages 4150–4159, 2019. 2, 3, 4, 5, 7, 8

[38] Xiaolong Wang, Ross Girshick, Abhinav Gupta, and Kaiming He. Non-local neural networks. In *Proceedings of the IEEE conference on computer vision and pattern recognition*, pages 7794–7803, 2018. 2

[39] Zhou Wang, Alan C Bovik, Hamid R Sheikh, Eero P Simoncelli, et al. Image quality assessment: from error visibility to structural similarity. *IEEE Transactions on Image Processing*, 13(4):600–612, 2004. 6

[40] Qi Wei, José Bioucas-Dias, Nicolas Dobigeon, and Jean-Yves Tourneret. Hyperspectral and multispectral image fusion based on a sparse representation. *IEEE Transactions on Geoscience and Remote Sensing*, 53(7):3658–3668, 2015. 2

[41] Qi Wei, José Bioucas-Dias, Nicolas Dobigeon, Jean-Yves Tourneret, Marcus Chen, and Simon Godsill. Multiband image fusion based on spectral unmixing. *IEEE Transactions on Geoscience and Remote Sensing*, 54(12):7236–7249, 2016. 2

[42] Zhuoyuan Wu, Jian Zhang, and Chong Mou. Dense deep unfolding network with 3d-cnn prior for snapshot compressive imaging. *arXiv preprint arXiv:2109.06548*, 2021. 4

[43] Qi Xie, Minghao Zhou, Qian Zhao, Zongben Xu, and Deyu Meng. Mhf-net: An interpretable deep network for multispectral and hyperspectral image fusion. *IEEE Transactions on Pattern Analysis and Machine Intelligence*, 2020. 1, 2, 3, 4, 5, 6, 7, 8

[44] Yang Xu, Zebin Wu, Jocelyn Chanussot, and Zhihui Wei. Nonlocal patch tensor sparse representation for hyperspectral image super-resolution. *IEEE Transactions on Image Processing*, 28(6):3034–3047, 2019. 1

[45] Fumihito Yasuma, Tomoo Mitsunaga, Daisuke Iso, and Shree K Nayar. Generalized assorted pixel camera: postcapture control of resolution, dynamic range, and spectrum. *IEEE Transactions on Image Processing*, 19(9):2241–2253, 2010. 6

[46] Minghao Yin, Zhuliang Yao, Yue Cao, Xiu Li, Zheng Zhang, Stephen Lin, and Han Hu. Disentangled non-local neural networks. In *European Conference on Computer Vision*, pages 191–207. Springer, 2020. 2

[47] Naoto Yokoya, Takehisa Yairi, and Akira Iwasaki. Coupled nonnegative matrix factorization unmixing for hyperspectral and multispectral data fusion. *IEEE Transactions on Geoscience and Remote Sensing*, 50(2):528–537, 2011. 2

[48] Roberta H Yuhas, Alexander FH Goetz, and Joe W Boardman. Discrimination among semi-arid landscape endmembers using the spectral angle mapper (sam) algorithm. 1992. 5

[49] Yongnian Zeng, Wei Huang, Maoguo Liu, Honghui Zhang, and Bin Zou. Fusion of satellite images in urban area: Assessing the quality of resulting images. In *2010 18th International Conference on Geoinformatics*, pages 1–4. IEEE, 2010. 6

[50] Jian Zhang and Bernard Ghanem. ISTA-Net: Interpretable optimization-inspired deep network for image compressive sensing. In *Proceedings of the IEEE conference on computer vision and pattern recognition*, pages 1828–1837, 2018. 4

[51] Kai Zhang, Min Wang, and Shuyuan Yang. Multispectral and hyperspectral image fusion based on group spectral embedding and low-rank factorization. *IEEE Transactions on Geoscience and Remote Sensing*, 55(3):1363–1371, 2016. 1, 3

[52] Lei Zhang, Wei Wei, Chengcheng Bai, Yifan Gao, and Yanning Zhang. Exploiting clustering manifold structure for hyperspectral imagery super-resolution. *IEEE Transactions on Image Processing*, 27(12):5969–5982, 2018. 1